Magnetic shepherding of nanocatalysts through hierarchically-assembled Fe-filled CNTs hybrids

Michele Melchionna[a], Alessandro Beltram[a], Antoine Stopin[b], Tiziano Montini[a,c], Rhys W. Lodge[d], Andrei N. Khlobystov[d], Davide Bonifazi[b,**], Maurizio Prato[a,e,f,*], Paolo Fornasiero[a,c,*]

[a] Department of Chemical and Pharmaceutical Sciences, University of Trieste and INSTM Trieste Research Unit, Via L. Giorgieri 1, 34127 Trieste, Italy
[b] School of Chemistry, Cardiff University, Park Place, Main Building, CF10 3AT, Cardiff, United Kingdom
[c] ICCOM-CNR URT, University of Trieste, Via L. Giorgieri 1, 34127 Trieste, Italy
[d] School of Chemistry, University of Nottingham, University Park, Nottingham, NG7 2RD, United Kingdom
[e] Carbon Nanobiotechnology Laboratory, CIC biomaGUNE, Paseo de Miramón 182, 20009 Donostia-San Sebastian, Spain
[f] Ikerbasque, Basque Foundation for Science, 48013 Bilbao, Spain

ARTICLE INFO

ABSTRACT

Mechanically robust, chemically stable and electronically active carbon nanotubes (CNTs) are widely used as supports in catalysis. Synergistic effects between CNT and the active phase critically depend on the homogeneity of the carbon/inorganic interface, whose assembly is difficult to achieve without admixtures of free-standing inorganic matrix. Here we show that Fe-filled CNTs, employed as nanocatalyst supports, allow a facile preparation of highly pure and uniform CNT/nanocatalyst materials, by taking advantage of magnetic separation from poorly-defined components (e.g. aggregates of inorganic nanocatalysts). The higher homogeneity translates into higher catalytic activity in two industrially important processes: the photocatalytic hydrogen production and the water-gas shift reaction, WGSR (increase of ~48% activity for the former and up to ~45% for the latter as compared to catalysts isolated by standard filtration). In addition, the magnetic Fe core in the nanotubes enables effective separation and re-use of the nanocatalyst without loss of activity. This study demonstrates significant potential of magnetic CNTs as next generation of sustainable catalyst supports that can improve production of hydrogen and reduce the use of precious metals.

1. Introduction

The introduction of a precise hierarchical order in the assembly of nanostructured materials is nowadays considered as the latest frontier in heterogeneous catalysis. Energy-related applications have particularly profited from the use of this concept [1,2]. The structural interplay of hierarchically organized phases is often the key factor for the achievement of notable boosts of catalytic performance in several chemical transformations [3]. In many cases, such interplay crucially depends on the interface, in particular a tight contact between the different components, which secures an efficient electronic communication and also underpins an enhanced robustness of the catalytically active sites [3]. The assembly of metal/metal oxide core-shell systems, where metal nanoparticles are enveloped within a layer of metal oxide phase, is an excellent demonstration of this important concept, showing improved activity and stability, arising from the enhanced contact between the two components [4].

Carbon nanotubes represent a very useful scaffold in modern nanostructured catalysts [5], having been combined with a range of inorganic counterparts, resulting in hierarchical nanohybrids with intriguing catalytic features [6]. For example, in photocatalytic processes the presence of CNTs in tight contact with the photoactive phase retard the recombination of the photogenerated holes and electrons, thus generating longer lived charge separated states, thanks to the electron scavenging ability of the graphitic scaffold [7]. On the other hand, in the WGSR, CNTs may help the electronic suppression of the deactivation pathway, with the catalytic performances depending on an optimum coverage of the carbon component with the active metal/metal oxide phase [8]. Many other examples are available where the beneficial role of CNTs is proven, and the critical importance of a close electronic crosstalk with the metal phase substantiated [9]. Despite the considerable advances in the preparation of CNT nanohybrids, a central and recurrent drawback lies in the generally poor control over the synthetic route to secure effective formation of a homogeneous

---

nanohybrid. In fact, synthesized CNTs-inorganic hybrids generally present considerable amounts of free-standing inorganic phase that [10], possessing lower activity, diminishes the catalytic efficiency of the hybrid materials. An attempt to reduce the admixtures of metal phase by simply decreasing the metal loading is not viable, as the coverage of the CNTs and the isolated aggregates formation proceed in parallel, and a decrease of the metal loading also leads to partly bare CNTs with resulting lowering of catalytic activity [8,11]. The development of a general and efficient strategy to maximize the interfacing between the CNTs and the inorganic active components while reducing the total amount of the metal phase would guarantee a step forward for the definitive establishment of CNT-based hybrid nanocatalysts. We conjectured that the shepherding of the more active CNT/metal nanostructures, liberated from post-synthetic CNT-free aggregates, could be the winning strategy, maximizing the catalytic potential by full exploitation of the CNT-inorganic phase interaction.

For their part, magnetic nanocatalysts have become an appealing alternative to standard catalysts, as they bring the great advantage of avoiding cost- and time-consuming protocols for filtration, separation and isolation from by-products [12–14] and an extra asset in the ease of the post-catalytic recovery step [15]. Some of us have previously reported the synthesis and characterization of multi-walled CNTs (MWCNTs) filled with a magnetic Fe phase (Fe@CNTs) [16] for use in cancer treatment and cell shepherding [17,18] as well as in electrocatalytic O_2 reduction and H_2 evolution [19]. Building on these concepts, here we describe the hierarchical assembly of Fe@CNTs/Pd@ MO_2 nanohybrid systems, integrating magnetic Fe@CNTs with an inorganic matrix made of Pd nanoparticles embedded within TiO_2 or CeO_2 nanocrystals. The magnetic Fe@CNTs core can harness a general and simple sieving process to obtain the most active CNT-based catalyst package as demonstrated by the measuring of the catalytic performances in two important energy-related processes: H_2 photocatalytic evolution and water-gas shift reaction (WGSR). Moreover, extension of the application of these nanohybrids to other chemical transformations may imply a direct involvement of the endohedral Fe phase, which can facilitate charge transfer pathways [20,21]. As a further asset of these new CNT-based hybrids, the recyclability of the catalyst can rely on the same simple principle of magnetic separation. We predict that the generality of our finding could spark new research on the use of a next generation of magnetic CNTs for heterogeneous catalytic applications.

2. Experimental

2.1. Synthesis of Fe@CNTs

The preparation of Fe@CNTs followed the procedure previously developed [19]. In detail: in a 180 cm long quartz tube of a furnace setup, a 10 cm long quartz substrate was introduced in the temperature region around 900 °C and a constant flow of 0.2 $m^3 h^{-1}$ of argon was used to purge the system of remaining air. Under this flux, ferrocene (5 g) was introduced in a boat and placed in a region close to 550 °C. Toluene vapour was then flown into the quartz tube of the furnace by the argon purge of 0.2 $m^3 h^{-1}$ for 15 min. The toluene flow is then turned off and the quartz substrate is moved to a cool zone of the 180 cm long quartz tube to allow the sample to cool down to room temperature under an argon flux of 0.2 $m^3 h^{-1}$. The black material is then washed with ethanol to remove any residual ferrocene to obtain pristine Fe@CNTs (about 2.3 g). The material was then subjected to HCl washing in order to remove any external Fe or Fe oxide. As produced Fe@MWCNTs (250 mg) was introduced into a 1 L round-bottomed flask with methanol (375 mL). The reacting mixture was sonicated for 10 min, an aqueous HCl solution (4 M, 125 mL) was added and the mixture was sonicated for 10 min and stirred for 24 h at room temperature. Water (375 mL) was added and the mixture filtered through a 0.45 μm hydrophobic polytetrafluoroethylene filter. The precipitate was redispersed by 10 min of sonication in 100 mL of methanol, filtered

through the same filter and washed with water (100 mL). This procedure was repeated twice. The precipitate obtained was then washed with methanol (few mL). A black powder (about 220 mg) was finally recovered.

2.2. Functionalization of Fe@CNTs with benzoic acid (f-Fe@CNTs)

Fe@CNTs (100 mg) were placed in a 500 mL round bottomed flask and N-methyl-2-pyrrolidone (NMP, 67 mL) was added. The solution was sonicated for 20 min and *p*-amino-benzoic acid (675 mg) was introduced, the solution was sonicated for another 10 min and diisopropylethylamine (DIPEA, 40 μL) was added. After 10 min of further sonication, isoamyl nitrite (1.5 mL) was added slowly and the reaction mixture was stirred at 90 °C for 20 h. The dispersion was cooled to room temperature and was filtered through 0.45 μm hydrophobic polytetrafluoroethylene filters. The precipitate was redispersed by 10 min of sonication in 100 mL of ethyl acetate and filtered through the same filter. This step was reproduced two additional times and the final precipitate was dispersed in 100 mL methanol by 10 min sonication, water (200 mL) was added and the suspension was filtered through the same filter. Two additional washings with water (50 mL) were also realized. The precipitate was finally washed with few mL of methanol to facilitate drying. About 85 mg of black powder (*f*-Fe@CNTs) were thus recovered.

2.3. Synthesis of Fe@CNTs/Pd@TiO_2-filt and Fe@CNTs/Pd@TiO_2-magn

The precursor Pd-MUA (MUA = mercapto-undecanoic acid) was prepared according to a previous procedure [22]. The *f*-Fe@CNTs were dispersed in absolute ethanol (EtOH mL/f-Fe@CNTs mg ratio: 2.5) by sonication for 30 min meanwhile a Pd-MUA THF solution (containing 1.5 mg of Pd) was slowly added to a THF solution of Ti(OBu)$_4$ (containing nominal 88.5 mg of TiO_2 respectively). Then the Pd@ TiO_2 precursor solution was slowly added under sonication to the *f*-Fe@CNTs dispersion and the mixture was further sonicated for 30 min. Finally a 10% solution of H_2O in EtOH (Ti(OBu)$_4$/H_2O molar ratio: 1/120) was dropped and the mixture sonicated for 30 min. The materials were collected by either magnetic separation (Fe@CNTs/PdTiO$_2$-magn) or by filtration (Fe@CNTs/PdTiO$_2$-filt). For the former, the dispersion was left in a vial close to a NdFeB magnet (purchased by www.supermagnete.it) for 3 h, the liquid phase was then discarded. This operation was repeated twice redispersing the material in fresh EtOH. The solid was then recovered and left to dry. For the filtration method, the dispersion was filtered on a 0.45 μm polytetrafluoroethylene Millipore membrane, washed with ethanol and dried overnight at 80 °C. The solids were thermally treated under a flow of H_2 (10%) in Argon (total flow 220 mL min^{-1}) for 5 h at 450 °C.

2.4. Synthesis of Fe@CNTs/Pd@CeO_2-filt and Fe@CNTs/Pd@CeO_2-magn

The synthesis was similar to the previous one used for TiO_2, with the exception that the Ce precursor was Ce(ODe)$_4$ (ODe = decyloxide), prepared according to a previously developed procedure [23]. In this case the thermal treatment was made in situ before the WGSR tests. The materials were treated under H_2 (10%) in Argon (total flow 49 mL min^{-1}) for 1 h at 250 °C.

The relative percentage of Pd@ MO_2 (M = Ti or Ce) was calculated based on TGA data. In particular, the Fe:CNT ratio was first evaluated and it was assumed that such ratio remains constant after hybridization with the Pd@ MO_2. After observing the CNT% in the final hybrid, the Fe proportion could therefore be calculated and the amount of Pd@ MO_2 evaluated by difference between the total inorganic residue and the Fe.

2.5. Characterization

Thermogravimetric analyses (TGA) of approximately 1 mg of each

compound is recorded on a TGA Q500 (TA Instruments) under air, by equilibrating at 100 °C for 20 min, and following a ramp of 10 °C min^{-1} up to 800 °C. Raman spectra are recorded with an inVia Renishaw microspectrometer equipped with Nd:YAG laser at 532 nm. To avoid sample damage or laser-induced heating/crystallization of the materials, the incident power was kept at 1% (full power of the laser is 100 mW). Powders are dispersed in EtOH, drop-cast onto a quartz slide and the solvent evaporated; at least 5 spectra per sample are recorded on different areas of the sample in order to check the uniformity of the materials. TEM was performed using a JEOL 2100F transmission electron microscope operating at 200 kV (field emission electron gun source, information limit 0.19 nm). TEM samples were prepared by casting several drops of methanolic suspensions onto a copper mesh or lacey carbon TEM grid and dried under ambient conditions. STEM images were acquired using a JEOL digital STEM system. EDX spectroscopy was performed using an Oxford Instruments XMax 80 T silicon drift detector with INCA Energy 250 Microanalysis system. Additional TEM images were acquired on a were performed on a TEM Philips EM208, using an acceleration voltage of 100 kV.

Textural properties have been analysed by N_2 physisorption at the liquid nitrogen temperature using a Micromeritics ASAP 2020 analyzer. Prior to the analysis, the samples have been degassed at 120 °C for 12 h. The surface area has been calculated adopting the Brunauer-Emmett-Teller (BET) model while the pore size distribution has been assessed following the Barrett-Joyner-Halenda (BJH) Analysis.

CO chemisorption experiments were carried out on CeO_2-based materials using a Micromeritics ASAP 2020C. Typically, 150 mg of the fresh material were loaded in a U-shaped reactor and reduced by flowing H_2(5%)/Ar (40 mL min^{-1}) at 120 °C for 1 h. The adsorbed hydrogen is then removed by evacuation at 250 °C for 6 h. Chemisorption analysis was performed firstly at 35 °C dosing CO (2–20 torr). A low pressure range has been employed to avoid carbonate formation on CeO_2-based materials. The contribution of physisorption was subtracted by the double-isotherm method. A CO/Pd stoichiometry of 1:1 has been employed to calculate the accessible fraction of the metal.

The effective composition of the prepared materials was determined by ICP-AES analysis after the optimization of an adequate dissolution procedure. To do that, 20 mg of the calcined samples were firstly heated in air at 600 °C within an Al_2O_3 crucible to burn the carbon-based structure. After that, the remaining powder was dissolved by a triacid attack (0.5 mL HF 48% + 0.5 mL HNO_3 65% + 0.1 mL $HClO_4$ 70%) at 80 °C for 2 h [24]. After dilution to 25 mL with water, the Fe, Ce, Ti and Pd concentrations were determined by ICP-AES analysis measuring the emission at 238.204, 413.764, 334.940 and 340.458 nm, respectively. Adequate calibration lines have been built using at least 5 points in the concentration range of the analysed metal, obtaining a $R^2 > 0.9995$.

X-Ray Absorption experiments were performed at the SAMBA beamline [25] of Synchrotron SOLEIL (France) with a Si (220) double crystal monochromator. The monochromator was kept fully tuned and harmonics were rejected by a pair of Pd-coated, Si mirrors. Spectra were measured in fluorescence mode using a 35-element Ge detector. One ionization chamber was used as the baseline monitor and two other chambers were used to continuously check the stability of the energy scale by placing a Fe foil as reference. The experiments were conducted loading 50 mg of the as-prepared $Fe@CNT/Pd@TiO_2$ material within the quartz capillary (thickness = 10 μm) between two quartz wool plugs. H_2(5%)/N_2 was flowed on the sample (30 mL min^{-1}) and the temperature was raised with a ramp of 5 °C min^{-1} using a gas blower. XANES/EXAFS spectra were recorded at the Fe K edge (7112 eV) in a continuous mode (1 full spectra every 2 min).

2.6. Photocatalytic tests

The materials were tested as photocatalyst for hydrogen production by photoreforming of an ethanol/water mixture (1/1 by volume) under two different light sources. A UV 125 W medium pressure Hg lamp

(model UV13F, Helios Italquartz, Italy) was used to illuminate a Pyrex photoreactor while a Teflon-lined photoreactor was illuminated with a Lot-Oriel Solar Simulator equipped with a 150 W Xe lamp and an Atmospheric Edge Filter with a cut-off at 300 nm. In a typical catalytic test, 10 mg of the calcined material was first suspended in the photoreactor by sonication for 10 min in 60 mL of ethanol solution and subsequently purged from air with Ar flow of 15 mL min^{-1} for 40 min and thermostated at 20 °C. During the purge and the catalytic test the materials were magnetically stirred. The on-line detection of volatile products was carried out using a Gas Chromatograph equipped with two analytical lines and a 10 way-two loops injection valve was employed for injection during on-line analysis of the gaseous products. In the former apparatus an Agilent 6890N Gas Chromatograph equipped with a MolSieve 5 Å (Restek, 30 m x 0.53 mm ID) column followed by a Thermal Conductivity Detector (TCD) was used for gaseous products quantification using Ar as carrier and a PoraPlot Q (Agilent, 30 m × 0.53 mm ID, 40 μm film) column using Ar as carrier followed by a methanator and a Flame Ionization Detector (FID) was employed for the detection of the volatile organic compounds. In the latter apparatus an Agilent 7890A Gas Chromatograph equipped with a Carboxen 1010 PLOT (Supelco, 30 m × 0.53 mm ID, 30 μm film) column followed by a Thermal Conductivity Detector (TCD) was used for gaseous products quantification using Ar as carrier and a DB–225 ms column (J&W, 60 m × 0.32 mm ID, 20 μm film) using He as carrier followed by a mass spectrometer (MS) HP 5975C for the detection of the volatile organic compounds.

2.7. WGSR tests

WGSR rates were measured in a tubular reactor at atmospheric pressure, using partial pressures of 7.6 Torr and 38 Torr each for CO and H_2O respectively. The gas hourly space velocity (GHSV) was set at 100000 h^{-1} using a total flow rate of 48.5 mL min^{-1} and 29 mg of the powdered catalyst. Water was introduced to the reactor by means of a Gas-Tight syringe, controlled by an infusion pump, while the partial pressures of CO and Ar were adjusted using mass flow controllers. The composition of the effluent from the reactor was monitored on-line using an Agilent 7890 gas chromatograph equipped with two analytical lines. A TCD detector, connected to a MolSieve 5 Å column using Ar as carrier, was used to monitor H_2 concentration while a FID detector, connected to a Select Permanent Gases/CO_2 column using He as carrier and a methanator, was used to monitor CO, CH_4 and CO_2.

3. Results and discussion

Our investigations started with the preparation of magnetic Fe@CNTs, enriched with α-Fe and Fe_3C, following a procedure previously developed by some of us [17]. Access to the hierarchical hybrids was attained through adaptation of a reported protocol [17]: the Fe@CNTs are covalently functionalized with benzoic acid units [18], which improve dispersibility in the polar liquid medium and serve as anchoring points for attaching the pre-assembled inorganic Pd-MUA@ $M(OR)_4$ precursor (MUA = mercaptoundecanoic acid, M = Ti or Ce, R = −Butyl or −Decyl). Controlled hydrolysis and magnetic separation afford the CNT-enriched nanohybrid (Fe@CNTs/Pd@MO_2-magn, Scheme 1). As a term of comparison, the corresponding catalyst separated by filtration was also prepared (Fe@CNTs/Pd@MO_2-filt). Two different metal oxides, each for a specific catalytic purpose, were chosen: TiO_2 as photoactive material in the photocatalytic hydrogen evolution and CeO_2 as an active support in the WGSR.

As a final treatment, a controlled thermal treatment of the as prepared nanohybrid allows stabilization of the inorganic component by crystallization of the oxide phase, and good accessibility to the Pd nanoparticles upon removal of the organic moieties used as protecting agents. In the case of the present materials, the thermal treatment has been performed under reducing conditions in flowing H_2/Ar (1:10)
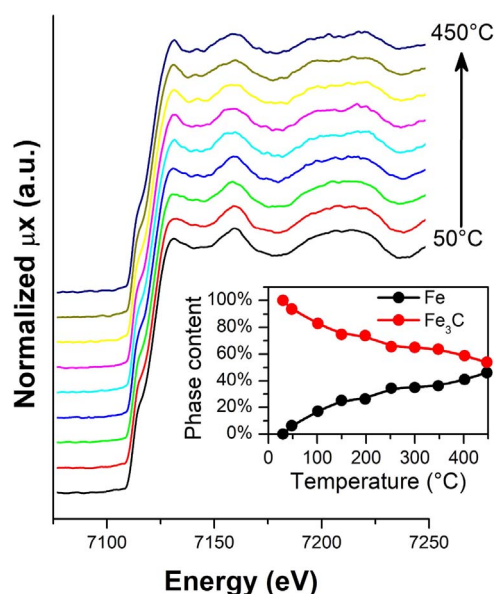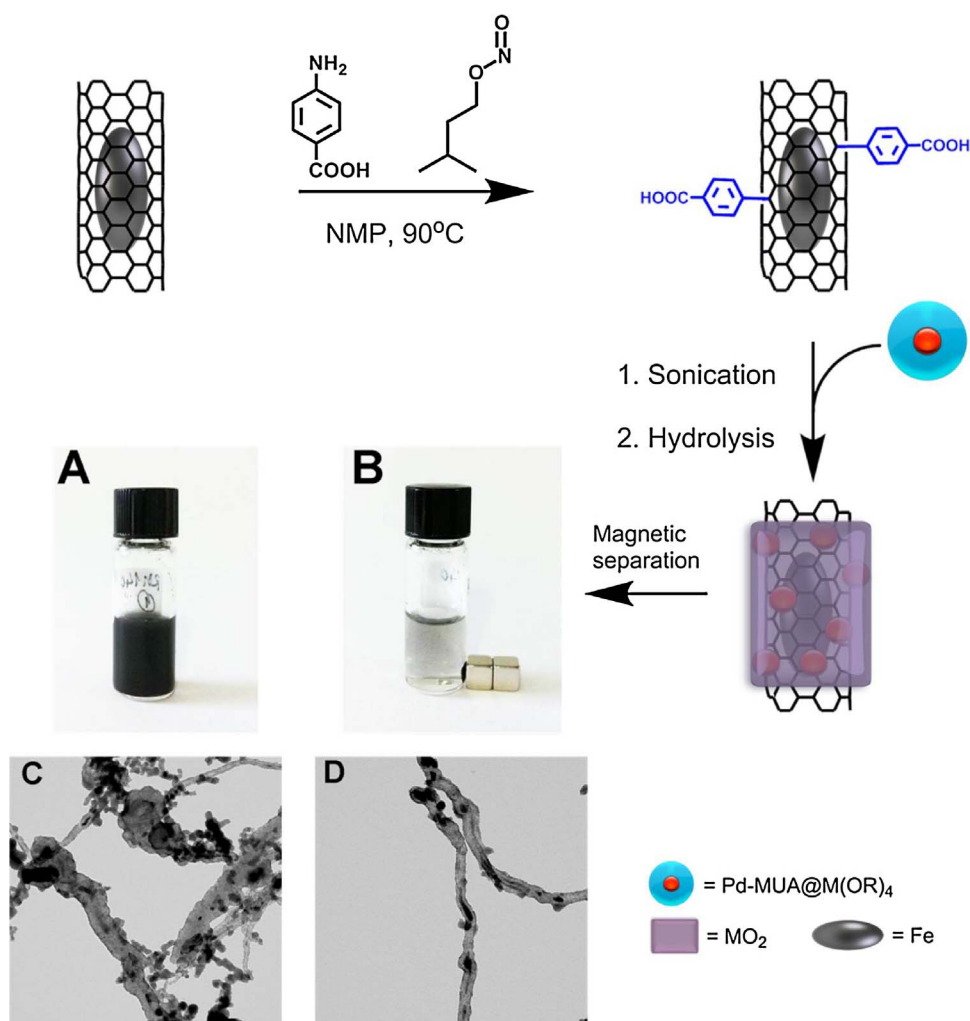
Fig. 1. XANES spectra at different temperatures recorded at the Fe K edge during treatment in H$_2$(5%)/N$_2$ of the Fe@CNTs/Pd@TiO$_2$-magn material. Inset: evolution of Fe$_3$C and Fe contents as derived from linear combination fitting of the XANES spectra.

instead of the previously employed oxidizing conditions (static air) [8]. XANES/EXAFS analysis of the Fe component (Fig. 1) revealed that, in the fresh materials, mainly Fe$_3$C is present, as also observed in the Fe@CNTs precursor by TEM and SAED inspection (Fig. S3). This is in agreement with our previous studies [17,19] and suggests that the coating procedure with the inorganic oxides did not affect the encapsulated magnetic component. Increasing the temperature during H$_2$ treatment, some subtle modifications appear in the XANES spectra, suggesting that Fe$_3$C is partially converted into Fe (see Fig. S1, part A). The contribution of the two components (Fe$_3$C and Fe) has been calculated by linear combination fitting of the XANES spectra acquired at different temperatures. Inset of Fig. 1 shows how the relative content of metallic Fe progressively increases at the reduction temperature increases up to 48% after reductive treatment at 450 °C (Fig. S1). Notably, no formation of FeO$_x$ was also observed during thermal treatment under H$_2$/Ar atmosphere. On the other hand, the formation of FeO$_x$ was observed when an oxidative treatment was applied at the same temperature (450 °C): the fitting of the XANES pattern (Fig. S2) revealed that the sample contains around 55 wt% of metallic Fe and 45% of γ-Fe$_2$O$_3$.

3.1. Fe@CNTs/Pd@TiO$_2$ for photocatalytic H$_2$ evolution

Prior to the catalytic tests, the material was subjected to a thermal treatment under H$_2$/Ar (1:10) flow at 450 °C to remove the organic ligands and crystallize the metal oxide. In this case, the reducing treatment is beneficial for titania-based material as it also causes an
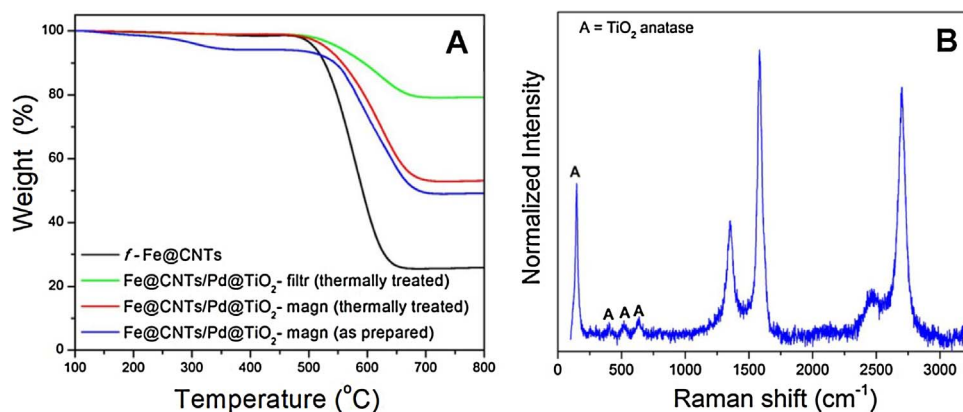
Fig. 2. Thermogravimetric analysis (TGA) of the TiO_2-based hybrids (A) and Raman spectrum of the thermally treated Fe@CNTs/Pd@TiO₂-magn (B).

enhancement of the photocatalytic activity due to the formation of Ti^{3+} centers associated with O vacancies [26–28]. Unfortunately, the quantification of the contribution of Ti^{3+} centers to catalysis could not be directly carried out for the present material. In fact, the corresponding thermal treatment of the magnetic catalyst in absence of H_2 (in order not to reduce Ti^{4+} species) resulted in concomitant oxidation of Fe, which compromises the catalytic activity. Thermogravimetric analysis (TGA) confirms that the two methods of isolation of the final material (magnetic separation vs filtration) lead to different CNT:inorganic weight ratios (0.85 and 0.24 for Fe@CNTs/Pd@TiO₂-magn and Fe@CNTs/Pd@TiO₂-filt, respectively) implying the presence of excess and free standing Pd@TiO₂ in the latter (Fig. 2A). From the analysis it can also be appreciated that in the as prepared material there is a small percentage of organic matter (combustion temperature ~250 °C), related to the organic ligands of the metal precursors, which is totally removed during the thermal treatment. Furthermore, the TGA of the *f*-Fe@CNTs shows that the residual Fe derivative accounts for about 23% (Fig. 2A).

Chemical analysis of the thermally treated materials performed by ICP-AES revealed the real composition of the obtained materials. The Fe@CNTs/Pd@TiO₂-filt sample composition is (by weight percent) Pd 1.01%, TiO_2 68.5% and Fe 7.23%, while the Fe@CNTs/Pd@TiO₂-magn sample contains Pd 0.57%, TiO_2 34.9% and Fe 15.1%. From these data, the carbon content was calculated as 23.3% and 49.4% for the filtered and magnetically separated materials, respectively. These values are larger than the weight loss observed during TGA (19.5% and 43.1% for Fe@CNTs/Pd@TiO₂-magn and Fe@CNTs/Pd@TiO₂-filt, respectively, Fig. 2A). This is due to the fact that Fe component is oxidized to Fe_2O_3 during TGA, accounting for the weight loss due to carbon burning and the weight gain due to Fe oxidation. However, the difference in CNT:inorganic ratio is not substantially altered by calculations based on ICP-AES analysis (0.98 for Fe@CNTs/Pd@TiO₂-magn vs 0.30 for Fe@CNTs/Pd@TiO₂-filt).

Raman analysis confirms that the CNT scaffold is retained after the calcination step, with the presence of the typical D and G bands respectively at ~ 1300 cm^{-1} and ~ 1590 cm^{-1}, together with the formation of TiO_2 anatase (bands at 198 cm^{-1}, 395 cm^{-1}, 513 cm^{-1} and 639 cm^{-1}) [29,30]. However, no bands associated to Fe oxides are found, further confirming the perfect isolation of the iron phase in the carbon nanotube cavity (Fig. 2B).

The homogeneous coverage of CNTs by TiO_2 incorporating Pd nanoparticles and the close contact between the CNT and inorganic components become evident through TEM analysis (Fig. 3A), which also indicates that encapsulation of Fe within the CNTs is retained after the synthetic procedure (Fig. 3B–C). Moreover, TEM inspection rules out any significant free-standing inorganic phase for Fe@CNTs/Pd@TiO₂-magn, while its presence is clearly observed for the Fe@CNTs/Pd@TiO₂-filt sample (Fig. S4). In addition, TEM analysis of the discarded liquid phase after magnetic purification of Fe@CNTs/

Pd@TiO₂-magn provides evidence of the presence of large TiO_2 aggregates (Fig. S5). EDX mapping confirms the presence and almost colocalization of C, Ti and O, with Fe encapsulated within CNTs (Fig. 3D–E). Fast Fourier Transform (FFT) additionally confirms that the TiO_2 is mostly in the anatase phase, contaminated with a tiny portion of rutile (Fig. S6). The higher element-dependent contrast of the HAADF images permits to clearly reveal the presence of the Pd nanoparticles (they appear as white compact dots due to the fact that Pd has the highest atomic number in this material) with a size distribution of 3.5 ± 0.6 nm (Fig. 3C and inset), also confirmed by the EDX analysis (Fig. S7).

It is interesting to note how the high temperature treatment does not cause agglomeration of Pd NPs into large aggregates, thanks to the protection ensured by the TiO_2 shell. A complete EDX mapping of all the elements together with a high resolution mapping of Pd and C reveal that the Pd nanoparticles are well dispersed along the CNT (Fig. 4).

The textural properties of both thermally-treated Fe@CNTs/Pd@TiO₂-magn and Fe@CNTs/Pd@TiO₂-filt, as well as those of the *f*-Fe@CNTs, were investigated by N_2 physisorption. All samples exhibit a type IV isotherm indicating extended mesoporous texture (Fig. S8). The main results from N_2 physisorption are summarized in Table 1. Despite the quite low surface areas of Fe@CNTs/Pd@TiO₂-magn and Fe@CNTs/Pd@TiO₂-filt (30 and 28 $m^2 g^{-1}$ respectively), the differences in the texture of the various materials are well evident. In particular, the hybrid materials show higher surface area (surface area of *f*-Fe@CNTs 17 $m^2 g^{-1}$) but lower pore volume than the *f*-Fe@CNT (0.074 and 0.050 $mL g^{-1}$ for the two hybrids vs 0.111 $mL g^{-1}$ for the *f*-Fe@CNTs, see Table 1). This is clearly related with the growth of the mesoporous Pd@TiO₂ layer, which is characterized by the presence of mesopores around 4 nm in the Barrett-Joyner-Halenda (BJH) pore distributions (Fig. S9).

The photocatalytic performance of the two thermally-treated catalysts was evaluated for the H_2 evolution from EtOH/H₂O solution under UV–vis irradiation. A comparison between the activities of the two materials undeniably displays a considerably superior performance of the Fe@CNTs/Pd@TiO₂-magn sample, reaching a stable H_2 productivity amounting to 1092 mmol $g_{Pd@TiO2}^{-1}$ after 20 h of irradiation, after normalization by the Pd@TiO₂ mass (Fig. 5A). In comparison, the Fe@CNTs/Pd@TiO₂-filt performance is about 46% lower (510 mmol $g_{Pd@TiO2}^{-1}$). The stability of both materials is pronounced, with steady H_2 production for at least 20 h of catalysis. The beneficial effect of the thermal treatment was also proven by comparing the activities of the as-prepared sample with those observed from the thermally treated material (Fig. S10), with the latter displaying an almost five-fold higher activity than the former. This effect is well known and is related to the crystallinity of the titania shell which bears an enhanced light absorption characteristics with lower band gaps than the amorphous TiO_2 [32]. As a term of comparison, the corresponding CNT-free catalyst (Pd@TiO₂) was also prepared and displayed even lower
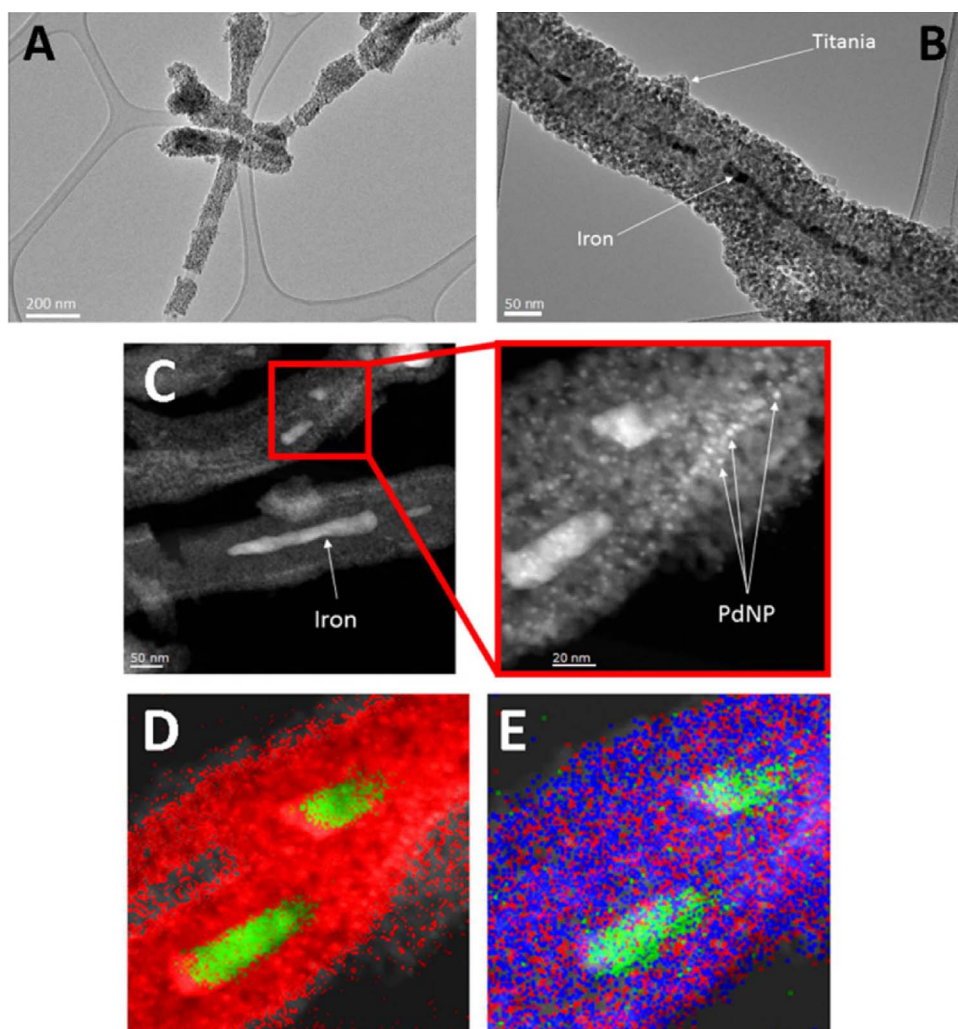
Fig. 3. A) low magnification and B) high magnification HRTEM and C) HAADF-STEM images of sample Fe@CNTs/Pd@TiO$_2$-magn thermally treated (inset of C: magnification showing the individual Pd NPs); D) EDX mapping showing carbon (red) and iron (green); E) EDX mapping showing titanium (blue), oxygen (red) and iron (green). (For interpretation of the references to colour in this figure legend, the reader is referred to the web version of this article.)
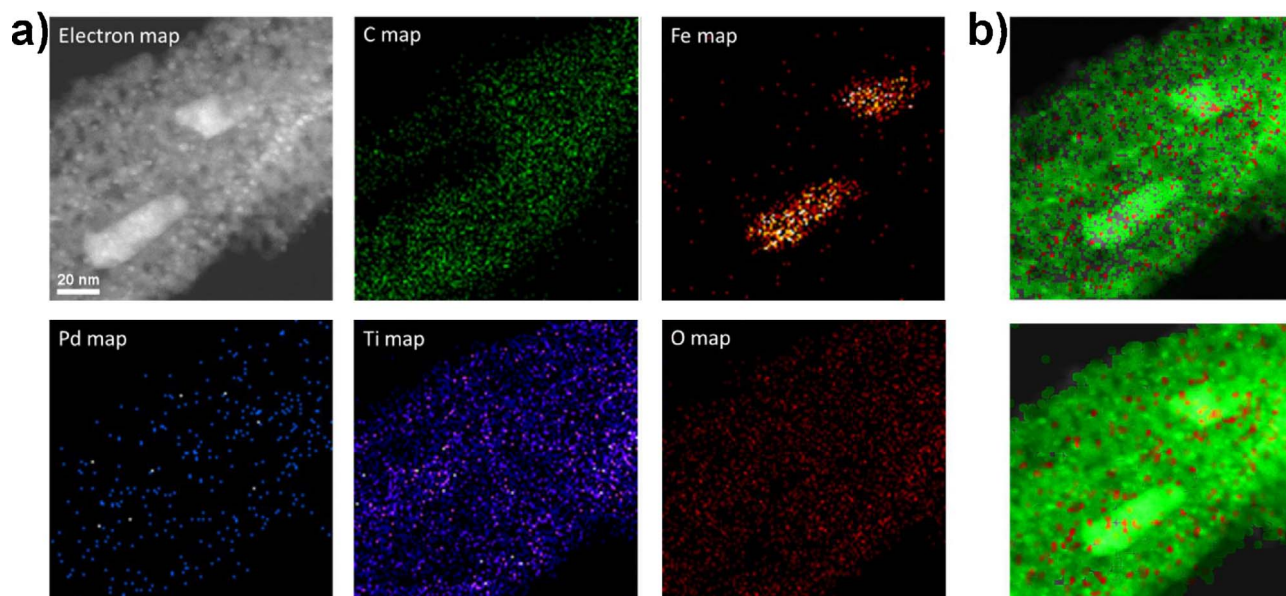
Fig. 4. a) HRTEM (top left) and EDX mapping of all the elements of Fe@CNTs/Pd@TiO$_2$-magn and b) High-resolution (top) and low-resolution (bottom) mapping of Pd nanoparticles (red) on carbon (green). (For interpretation of the references to colour in this figure legend, the reader is referred to the web version of this article.)

Table 1
Summary of results from analysis of the N_2 physisoprtion isotherms of the TiO_2-based samples.

Sample	$f - Fe@CNTs$	Fe@CNTs/ Pd@TiO$_2$- magn (thermally treated)	Fe@CNTs/ Pd@TiO$_2$- filtr (thermally treated)
Type of isotherm [a]	II	IV	IV
Specific Surface Area (m²/g) [b]	17	30	28
Cumulative Pore Volume (mL/ g) [c]	0.111	0.074	0.050
D_{max} (nm) [d]	77	4.0/113	3.7/95

[a] Accordingly to IUPAC recommendation [31].

[b] Calculated using the BET equation.

[c] Calculated from the BJH analysis of the desorption branch of the N_2 physisorption isotherms.

[d] Maximum of the pore size distribution obtained applying the BJH analysis to the adsorption branch of the N_2 physisorption isotherms, reported in Fig. S9.

activity, indicating the benefits of including CNT in the catalyst formulation. A comparison with Fe-free analogues cannot be done as it is misleading, due to the fact that it is not possible to prepare uniformly covered CNTs without the presence of additional isolated Pd@MO$_2$ component (whose percentage content is not measurable), making the direct comparison affected by a considerable bias.

The magnetic properties of the nanotubes can also be exploited for the post catalytic recovery of the catalyst. Recycling tests based on magnetic separation from the liquid phase after 3 cycles of simulated solar irradiation shows no significant decrease of activity. This implies that the material preserves its structural and catalytic characteristics and that the magnetic recovery method is simple, robust and reproducible (Fig. 5B).

3.2. Fe@CNTs/Pd@CeO$_2$ for WGSR

As a further proof of the key importance of the homogeneity of the CNT hybrids, the synthesis and performance towards the WGSR (CO + H$_2$O ↔ H$_2$ + CO$_2$) of Fe@CNTs/Pd@CeO$_2$ was evaluated. In this case, CeO$_2$ was chosen as a metal oxide layer given its well-known promoting effect for catalytic WGSR [33]. The advantages of integrating CNTs with Pd@CeO$_2$ in the WGSR have been recently proved [34], and in particular it been highlighted that an optimum CeO$_2$/CNT ratio, that causes the most homogeneous coverage of the carbon scaffold, also reflects in a superior catalytic activity and stability [8].

The as prepared hybrids were first compared based on their composition, obtained from TGA and ICP-AES data. TGA analysis in air flow of the as prepared materials show a 2-step weight loss, the first one (around 200 °C) related with removal of organic capping agents and the second one (from 400 to 600 °C) due to combustion of CNT scaffold (Fig. 6A). ICP-AES analysis revealed that the composition of the thermally treated materials are Pd 1.31%, CeO$_2$ 69.5%, Fe 7.30% and C 21.9% for Fe@CNTs/Pd@CeO$_2$-magn and Pd 1.65%, CeO$_2$ 84.8%, Fe 3.75% and C 9.80% for Fe@CNTs/Pd@CeO$_2$-filt. Also in this case, the real C content is higher than the weight loss detected by TGA in air in the range 400–600 °C (19.05% and 8.15% for magnetically separated and filtered samples, respectively), since Fe oxidation results in a gain in the weight of the sample that superimposes to the weight loss due to CNT combustion. As in the previous case, a higher CNT:inorganic weight ratio (0.28 vs 0.11) for the magnetically purified material has been observed (based on the more accurate ICP-AES analysis).

Raman analysis shows no signal relative to the CeO$_2$, indicating that the as-prepared material contains amorphous ceria. Increasing laser power causes local crystallization and the signature band of crystalline CeO$_2$ appears (Fig. 6B) [35]. The Raman spectrum of the material after the thermal treatment (Fig. S11) reveals large presence of CeO$_2$, while no obvious signal attributed to Ce^{3+} is noted (although the presence of Ce^{3+} cannot be ruled out on the basis of the Raman, as the signal may be comparatively much lower).

As in the case of the TiO$_2$-based material, TEM shows that the resulting nanohybrid structure reveals a uniform coverage of the CNT backbone with the inorganic matter. However, while the Fe@CNTs/Pd@CeO$_2$-magn sample does not present any free standing inorganic aggregate following a thorough TEM inspection (Fig. 7A–B), the Fe@CNTs/Pd@CeO$_2$-filt catalyst isolation is accompanied by a relatively high density of islands of free standing Pd@CeO$_2$ (Fig. 7C-D).

CO chemisorption has been employed to evaluate Pd accessibility after thermal treatment of the samples under H$_2$/Ar atmosphere. The analysis revealed a CO/Pd ratio of 0.271 for Fe@CNTs/Pd@CeO$_2$-magn and of 0.241 for Fe@CNTs/Pd@CeO$_2$-filt. These values are in good agreement with what was observed for other prepared materials starting for the Pd@CeO$_2$ core-shell units supported on either silanized Al$_2$O$_3$ [4] or decorating CNT [8]. Since comparable Pd accessibility has been observed for both the materials, the optimal organization of the Pd@CeO$_2$ units around the CNTs scaffold does not seem to be crucial to obtain a good accessibility of the Pd active phase.

The activity of the present materials with respect to the WGSR process has been evaluated analysing the CO conversion rate at different temperatures (200, 250, 275, 300 °C), maintaining each thermal treatment for 4 h. In the present case, the thermal pre-treatment of the two catalysts Fe@CNTs/Pd@CeO$_2$-filt and Fe@CNTs/Pd@CeO$_2$-magn
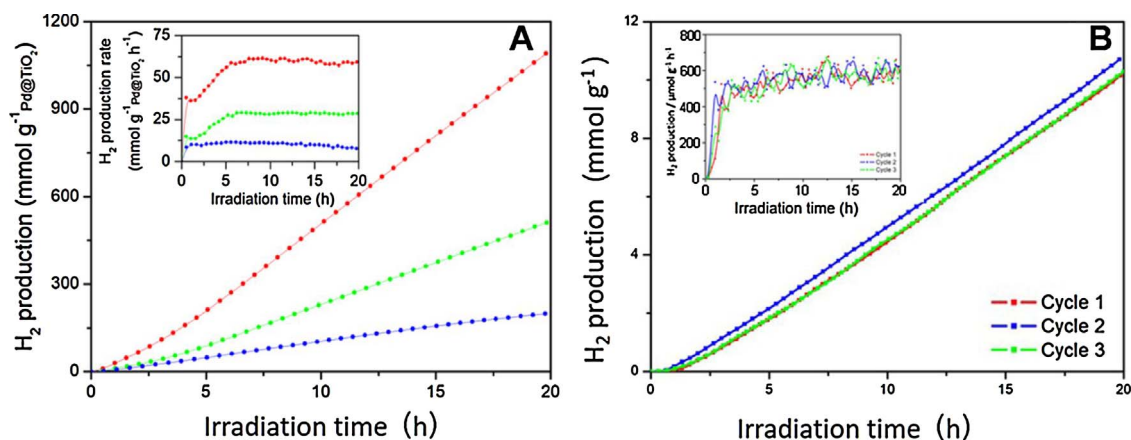
Fig. 5. A) Photocatalytic H$_2$ production over 20 h under UV irradiation by the thermally treated Fe@CNTs/Pd@TiO$_2$-magn (red), Fe@CNTs/Pd@TiO$_2$-filt (green) and CNT-free Pd@TiO$_2$ (blue) normalized by the Pd@TiO$_2$ content. Inset: H$_2$ evolution rates. B) Photocatalytic H$_2$ production under simulated solar light by the thermally treated Fe@CNTs/Pd@TiO$_2$-magn over three cycles after magnetic recovery of the catalysts. Inset: H$_2$ evolution rates. (For interpretation of the references to colour in this figure legend, the reader is referred to the web version of this article.)
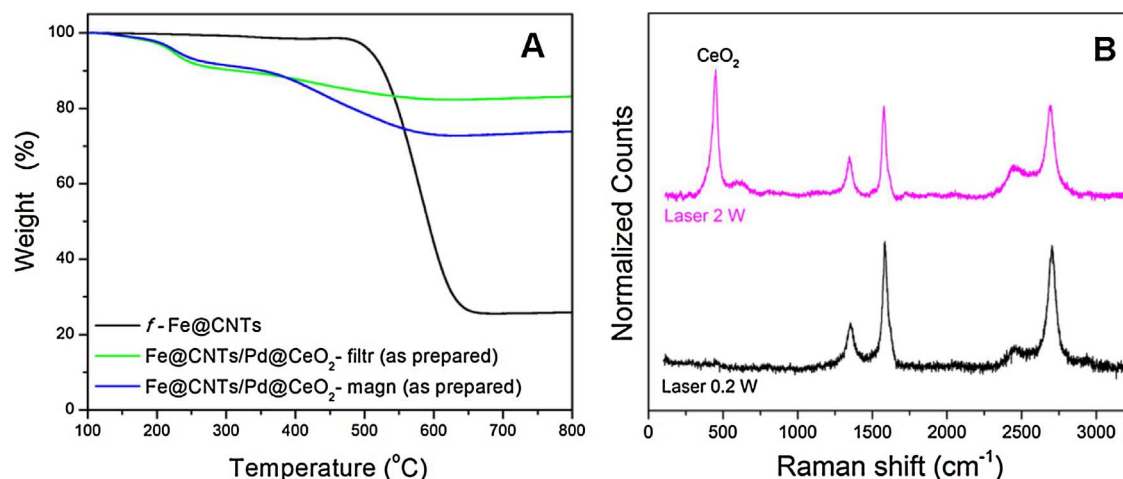
Fig. 6. A) Thermogravimetric analysis (TGA) and B) Raman spectra of the CeO$_2$-based hybrids.

was carried out *in situ* prior to the catalytic tests, by heating the material under H$_2$/Ar flow at 250 °C for 1 h. At each temperature, the catalysts displayed a stable CO conversion for the investigated time and, notably, an enhancement of the conversion rate of Fe@CNTs/Pd@CeO$_2$-magn compared to Fe@CNTs/Pd@CeO$_2$-filt was observed (Fig. 8). Remarkably, the gap in terms of CO conversion rate between both materials increases with the temperature in favor of the latter, the performances for the magnetically purified sample being almost doubled with respect to that filtered one at 300 °C. No other by-products such as CH$_4$ were revealed in GC analysis, indicating that

hydrogenation processes are negligible under the present experimental conditions. In accordance with our previous results [8], the presence of the CNT in the catalyst formulation provides an improved over time stability in the WGSR, as compared with the Pd@CeO$_2$ catalyst, which has similar activity but worse stability.

The present results highlight the importance of the optimization of the contact between the carbon nanomaterial and the inorganic active phase on the control of the activity of the final hybrid material. With respect to the WGSR process, our previous studies revealed that Pd@CeO$_2$ units deposited on an insulating support (Al$_2$O$_3$) rapidly
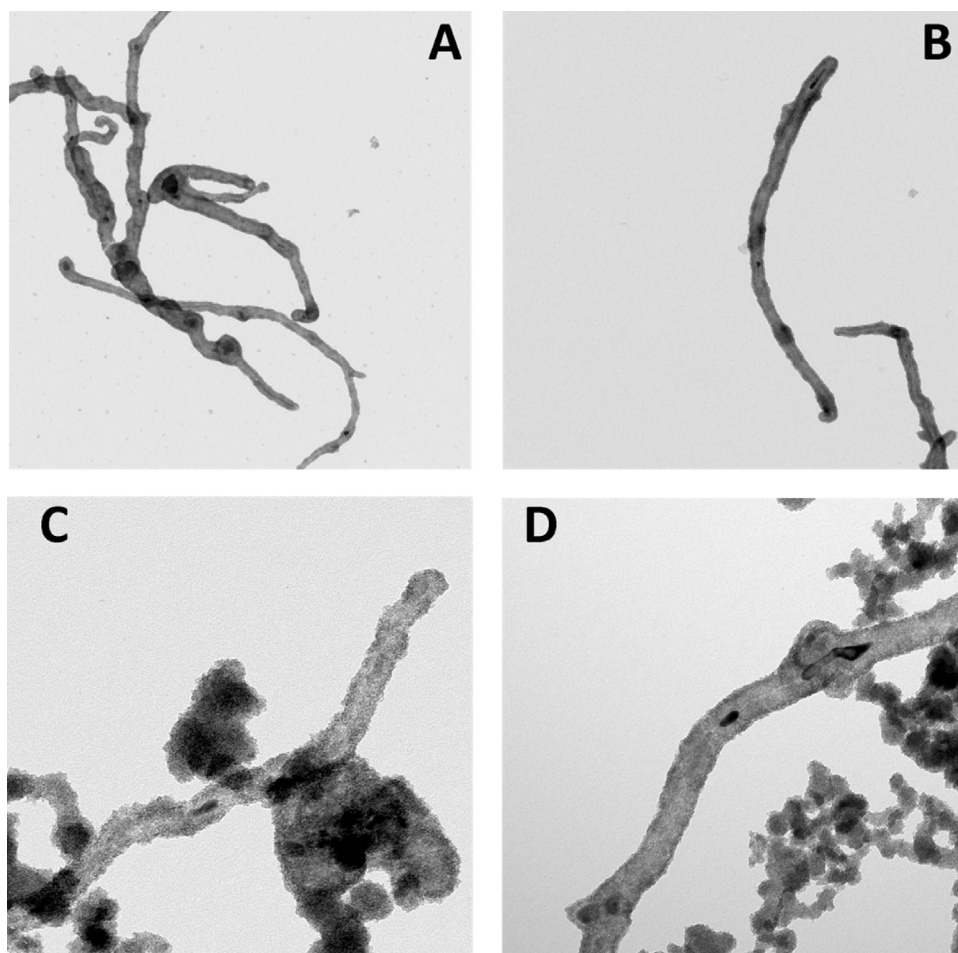

Fig. 7. A) and B) Representative TEM images of Fe@CNTs/Pd@CeO$_2$-magn showing the good coverage and homogeneity of the material; C) and D) Representative TEM images of Fe@CNTs/Pd@CeO$_2$-filt showing presence of free standing aggregates made of Pd@CeO$_2$.
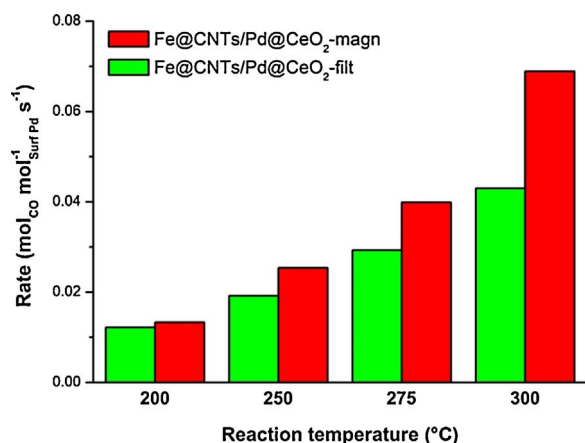
Fig. 8. Rate of CO conversion of CeO_2-based materials at different temperatures normalized by the accessible Pd content.

deactivates due to a combination of physical and electronic deactivation [36]: the CO adsorption on Pd nanoparticles is hindered after deep reduction of CeO_2, by occlusion of the small mesopores after expansion of CeO_2 crystal lattice and by electronic deactivation from reduced CeO_2. The formation of hybrid composite materials employing oxidized CNT as scaffolds for directing the assembly of $Pd@CeO_2$ units leads to an improved stability [34], although with a decreased activity. The improvement of stability was related with the electronic properties of the CNT scaffold that helps in draining the excess charge deriving from CeO_2 reduction. A further development in terms of performances was obtained by *ad hoc* functionalization of CNTs to preserve their electronic conductivity and by applying a moderate thermal treatment to improve the textural properties of the composite [8]. The results presented in this study further confirm the importance of producing materials with an optimized intimate contact between the CNTs scaffold and the $Pd@CeO_2$ matrix. In this case, the magnetic core provides a unique tool to purify CNTs homogeneously covered by $Pd@CeO_2$ from the free standing inorganic phase, finally leading to the material with the more intimate contact between the two components.

4. Conclusions

The key role of CNTs in catalytic applications featuring nanostructured hybrid materials is directly demonstrated by utilizing a new concept based on magnetic sieving of the Fe-filled nanostructures. By this means, the final hybrid material is liberated of post-synthetic unreacted metallic matter that have so far represented a notorious problem, affecting intrinsic performances of the hybrid catalyst as well as the reproducibility of results. The new strategy, in contrast, allows for extremely homogeneous material where the contact CNT/metal oxide is maximized. In turn, this results in higher intrinsic performance, as demonstrated with two important catalytic processes such as photocatalytic hydrogen production (increase of ~46%) and WGSR (up to ~45%) for the two examples examined in this work. Our new approach has also the potential to mitigate the uncertainty of reported results involving CNT-based heterogeneous catalysts, as it provides a pathway to access structurally better defined hybrid, making future comparisons of activity more meaningful. Given the versatile preparative protocol and low-cost production of Fe-filled CNTs, we anticipate that the concept put forward in this paper can be adapted to prepare novel nanocatalysts for other heterogeneous processes.

Acknowledgements

Appendix A. Supplementary data

Supplementary data associated with this article can be found, in the online version, at https://doi.org/10.1016/j.apcatb.2018.01.049.

References

[1] F. Wang, T.A. Shifa, X. Zhan, Y. Huang, K. Liu, Z. Cheng, C. Jiang, J. He, Recent advances in transition-metal dichalcogenide based nanomaterials for water splitting, Nanoscale 7 (2015) 19764–19788.
[2] P. Trogadas, V. Ramani, P. Strasser, T.F. Fuller, M.-O. Coppens, Hierarchically structured nanomaterials for electrochemical energy conversion, Angew. Chem. Int. Ed. 55 (2016) 122–148.
[3] Y. Yamada, C.-K. Tsung, W. Huang, Z. Huo, S.E. Habas, T. Soejima, C.E. Aliaga, G.A. Somorjai, P. Yang, Nanocrystal bilayer for tandem catalysis, Nat. Chem. 3 (2011) 372–376.
[4] M. Cargnello, J.J.D. Jaén, J.C.H. Garrido, K. Bakhmutsky, T. Montini, J.J.C. Gámez, R.J. Gorte, P. Fornasiero, Exceptional activity for methane combustion over modular $Pd@CeO_2$ subunits on functionalized Al_2O_3, Science 337 (2012) 713–717.
[5] D.S. Su, S. Perathoner, G. Centi, Nanocarbons for the development of advanced catalysts, Chem. Rev. 113 (2013) 5782–5816.
[6] D. Eder, Carbon nanotube-Inorganic hybrids, Chem. Rev. 110 (2010) 1348–1385.
[7] K. Woan, G. Pyrgiotakis, W. Sigmund, Photocatalytic Carbon-Nanotube–TiO_2 composites, Adv. Mater. 21 (2009) 2233–2239.
[8] A. Beltram, M. Melchionna, T. Montini, L. Nasi, R.J. Gorte, M. Prato, P. Fornasiero, Improved activity and stability of $Pd@CeO_2$ core-shell catalysts hybridized with multi-walled carbon nanotubes in the water gas shift reaction, Catal. Today 253 (2015) 142–148.
[9] M. Melchionna, M. Bonchio, F. Paolucci, M. Prato, P. Fornasiero, Catalysis-material crosstalk at tailored nano-carbon interfaces, Top. Curr. Chem. 348 (2014) 139–180.
[10] A. Singh, A. Chandra, Significant performance enhancement in asymmetric supercapacitors based on metal oxides, carbon nanotubes and neutral aqueous electrolyte, Sci. Rep. 5 (2015) 15551.
[11] A. Beltram, M. Melchionna, T. Montini, L. Nasi, P. Fornasiero, M. Prato, Making H_2 from light and biomass-derived alcohols: the outstanding activity of newly designed hierarchical MWCNT/$Pd@TiO_2$ hybrid catalysts, Green Chem. 19 (2017) 2379–2389.
[12] M.B. Gawande, R. Luque, R. Zboril, The rise of magnetically recyclable nanocatalysts, ChemCatChem 6 (2014) 3312–3313.
[13] A. Schätz, T.R. Long, R.N. Grass, W.J. Stark, P.R. Hanson, O. Reiser, Immobilization on a nanomagnetic Co/C surface using ROM polymerization: generation of a hybrid material as support for a recyclable palladium catalyst, Adv. Funct. Mater. 20 (2010) 4323–4328.
[14] S. Shylesh, V. Schünemann, W.R. Thiel, Magnetisch abtrennbare Nanokatalysatoren: brücken zwischen homogener und heterogener Katalyse, Angew. Chem. 122 (2010) 3504–3537.
[15] V. Polshettiwar, R. Luque, A. Fihri, H. Zhu, M. Bouhrara, J.-M. Basset, Magnetically recoverable nanocatalysts, Chem. Rev. 111 (2011) 3036–3075.
[16] A. Stopin, F. Pineux, R. Marega, D. Bonifazi, Magnetically active carbon nanotubes at work, Chem. Eur. J. 21 (2015) 9288–9301.
[17] F. Pineux, R. Marega, A. Stopin, A. La Torre, Y. Garcia, E. Devlin, C. Michiels, A.N. Khlobystov, D. Bonifazi, Biotechnological promises of Fe-filled CNTs for cell shepherding and magnetic fluid hyperthermia applications, Nanoscale 7 (2015) 20474–20488.
[18] R. Marega, F. De Leo, F. Pineux, J. Sgrignani, A. Magistrato, A.D. Naik, Y. Garcia, L. Flamant, C. Michiels, D. Bonifazi, Functionalized Fe-Filled multiwalled carbon nanotubes as multifunctional scaffolds for magnetization of cancer cells, Adv. Funct. Mater. 23 (2013) 3173–3184.
[19] M.V. Bracamonte, M. Melchionna, A. Stopin, A. Giulani, C. Tavagnacco, Y. Garcia, P. Fornasiero, D. Bonifazi, M. Prato, Carboxylated, Fe-filled multiwalled carbon nanotubes as versatile catalysts for O_2 reduction and H_2 evolution reactions at physiological pH, Chem. Eur. J. 21 (2015) 12769–12777.
[20] D. Deng, L. Yu, X. Chen, G. Wang, L. Jin, X. Pan, J. Deng, G. Sun, X. Bao, Iron encapsulated within pod-like carbon nanotubes for oxygen reduction reaction, Angew. Chem. Int. Ed. 52 (2013) 371–375.
[21] X. Yang, X. Yu, H. Peng, H. Wang, Confined iron nanowires enhance the catalytic activity of carbon nanotubes in the aerobic oxidation of cyclohexane, ChemSusChem 5 (2012) 1213–1217.
[22] K. Bakhmutsky, N.L. Wieder, M. Cargnello, B. Galloway, P. Fornasiero, R.J. Gorte, A versatile route to core-shell catalysts: synthesis of dispersible M@oxide (M = Pd Pt; oxide = TiO_2, ZrO_2) nanostructures by self-assembly, ChemSusChem 5 (2012) 140–148.
[23] M. Cargnello, N.L. Wieder, T. Montini, R.J. Gorte, P. Fornasiero, Synthesis of dispersible $Pd@CeO_2$ core-shell nanostructures by self-assembly, J. Am. Chem. Soc.

132 (2010) 1402–1409.

[24] M. Tella, M. Auffan, L. Brousset, J. Issartel, I. Kieffer, C. Pailles, E. Morel, C. Santaella, B. Angeletti, E. Artells, J. Rose, A. Thiéry, J.-Y. Bottero, Transfer, transformation, and impacts of ceria nanomaterials in aquatic mesocosms simulating a pond ecosystem, Environ. Sci. Technol. 48 (2014) 9004–9013.

[25] V. Briois, E., Fonda, S., Belin, L., Barthe, C. La Fontaine, F., Langlois, M., Ribbens, F. Villain, SAMBA: The 4–40 keV X-ray absorption spectroscopy beamline at SOLEIL, UVX 2010 − 10e Colloque sur les Sources Cohérentes et Incohérentes UV, VUV et X; Applications et Développements Récents, 2011 41–47.

[26] X. Liu, G. Zhu, X. Wang, X. Yuan, T. Lin, F. Huang, Progress in black titania: a new material for advanced photocatalysis, Adv. Energy Mater 6 (2016) 1600452.

[27] X. Chen, L. Liu, F. Huang, Black titanium dioxide (TiO$_2$) nanomaterials, Chem. Soc. Rev. 44 (2015) 1861–1885.

[28] A. Naldoni, M. Allieta, S. Santangelo, M. Marelli, F. Fabbri, S. Cappelli, C.L. Bianchi, R. Psaro, V. Dal Santo, Effect of nature and location of defects on bandgap narrowing in black TiO$_2$ nanoparticles, J. Am. Chem. Soc. 134 (2012) 7600–7603.

[29] O. Frank, M. Zukalova, B. Laskova, J. Kurti, J. Koltai, L. Kavan, Raman spectra of titanium dioxide (anatase rutile) with identified oxygen isotopes (16,17,18), Phys. Chem. Chem. Phys. 14 (2012) 14567–14572.

[30] T. Ohsaka, F. Izumi, Y. Fujiki, Raman spectrum of anatase, TiO$_2$, J. Raman Spectrosc. 7 (1978) 321–324.

[31] K.S.W. Sing, Reporting physisorption data for gas/solid systems with special reference to the determination of surface area and porosity (Recommendations 1984), Pure Appl. Chem. (1985) 603.

[32] C.P. Lin, H. Chen, A. Nakaruk, P. Koshy, C.C. Sorrell, Effect of annealing temperature on the photocatalytic activity of TiO$_2$ thin films, Energy Procedia 34 (2013) 627–636.

[33] T. Montini, M. Melchionna, M. Monai, P. Fornasiero, Fundamentals and catalytic applications of CeO$_2$-based materials, Chem. Rev. 116 (2016) 5987–6041.

[34] M. Cargnello, M. Grzelczak, B. Rodríguez-González, Z. Syrgiannis, K. Bakhmutsky, V. La Parola, L.M. Liz-Marzán, R.J. Gorte, M. Prato, P. Fornasiero, Multiwalled carbon nanotubes drive the activity of metal@oxide core–shell catalysts in modular nanocomposites, J. Am. Chem. Soc. 134 (2012) 11760–11766.

[35] J.E. Spanier, R.D. Robinson, F. Zhang, S.-W. Chan, I.P. Herman, Size-dependent properties of CeO$_{2-y}$ nanoparticles as studied by Raman scattering, Phys. Rev. B 64 (2001) 245407.

[36] N.L. Wieder, M. Cargnello, K. Bakhmutsky, T. Montini, P. Fornasiero, R.J. Gorte, Study of the water-gas-shift reaction on Pd@CeO$_2$/Al$_2$O$_3$ core-shell catalysts, J. Phys. Chem. C 115 (2011) 915–919.